Case Studies in Thermal Engineering 34 (2022) 102049

Contents lists available at ScienceDirect

Case Studies in Thermal Engineering

journal homepage: www.elsevier.com/locate/csite

Nanofluid mixed convection inside wavy cavity with heat source: A non-homogeneous study

Ammar I. Alsabery [a], Mohammad Vaezi [b], Tahar Tayebi [c,d], Ishak Hashim [e,*], Mohammad Ghalambaz [f,g], Ali J. Chamkha [h]

[a] Refrigeration & Air-conditioning Technical Engineering Department, College of Technical Engineering, The Islamic University, Najaf, Iraq
[b] K. N. Toosi University of Technology, Iran
[c] Faculty of Sciences and Technology, Mohamed El Bachir El Ibrahimi University, Bordj Bou Arreridj, El-Anasser, Algeria
[d] Energy Physics Laboratory, Department of Physics, Faculty of Science, Mentouri Brothers Constantine1 University, Constantine, Algeria
[e] Department of Mathematical Sciences, Faculty of Science & Technology, Universiti Kebangsaan Malaysia, 43600, UKM Bangi, Selangor, Malaysia
[f] Metamaterials for Mechanical, Biomechanical and Multiphysical Applications Research Group, Ton Duc Thang University, Ho Chi Minh City, 758307, Viet Nam
[g] Faculty of Applied Sciences, Ton Duc Thang University, Ho Chi Minh City, 758307, Viet Nam
[h] Faculty of Engineering, Kuwait College of Science and Technology, Doha District, 35001, Kuwait

GRAPHICAL ABSTRACT

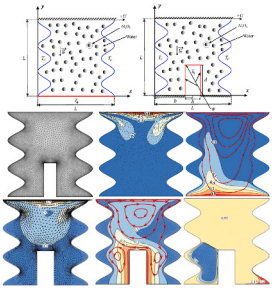

ARTICLE INFO

Keywords:
Nanofluid
Mixed convection
Wavy cavity
Thermophoresis and brownian motion
Heat source
EFM

ABSTRACT

In this study, mixed convection regarding nanofluid within the wavy lid-driven enclosure and a prominent heat source is investigated. A two-phase method is applied to the employed nanoliquid which leads to a non-homogeneous concentration field. The obtained governing equations are solved by the finite element technique. The effects of adding nanoparticles in base flow on velocity, temperature, and concentration field are investigated. Also, the effects of different geometric dimensions on heat transfer, such as heat source aspect ratio, wave number, and amplitude

* Corresponding author.
E-mail address: ishak_h@ukm.edu.my (I. Hashim).

https://doi.org/10.1016/j.csite.2022.102049
Received 7 September 2021; Received in revised form 9 April 2022; Accepted 16 April 2022
Available online 25 April 2022

of wavy walls are investigated. The outcomes reveal that increasing the application of nanoparticles, wave number and amplitude of the wavy wall, and aspect ratio of heat source yields an improvement within the rate of heat transfer.

Nomenclature

A	amplitude
AR	aspect ratio of the heat source, $AR = D/H$
B	dimensionless heat source position, $B = b/L$
C_p	specific heat capacity
D	dimensionless heat source length, $D = d/L$
d_f	diameter of the base fluid molecule
d_p	diameter of the nanoparticle
D_B	Brownian diffusion coefficient
D_{B0}	reference Brownian diffusion coefficient
D_T	thermophoretic diffusivity coefficient
D_{T0}	reference thermophoretic diffusion coefficient
H	dimensionless width of the heat source, $H = h/L$
k	thermal conductivity
L	width and height of the square cavity
Le	Lewis number
N	number of undulations
N_{BT}	ratio of Brownian to thermophoretic diffusivity
$\overline{Nu}$	average Nusselt number
Pr	Prandtl number
Ri	Richardson number
Re_B	Brownian motion Reynolds number
Sc	Schmidt number
T	temperature
T_0	reference temperature (310K)
T_{fr}	freezing point of the base fluid (273.15K)
$\mathbf{v}$	velocity vector
$\mathbf{V}$	normalized velocity vector
u_B	Brownian velocity of the nanoparticle
x, y & X, Y	space coordinates & dimensionless space coordinates

Greek symbols

α	thermal diffusivity
γ	inclination angle of magnetic field
β	thermal expansion coefficient
δ	normalized temperature parameter
θ	dimensionless temperature
μ	dynamic viscosity
ν	kinematic viscosity
ρ	density
φ	solid volume fraction
φ^*	normalized solid volume fraction
φ	average solid volume fraction

Subscript

b	bottom
c	cold
f	base fluid
h	hot
nf	nanofluid
p	solid nanoparticles

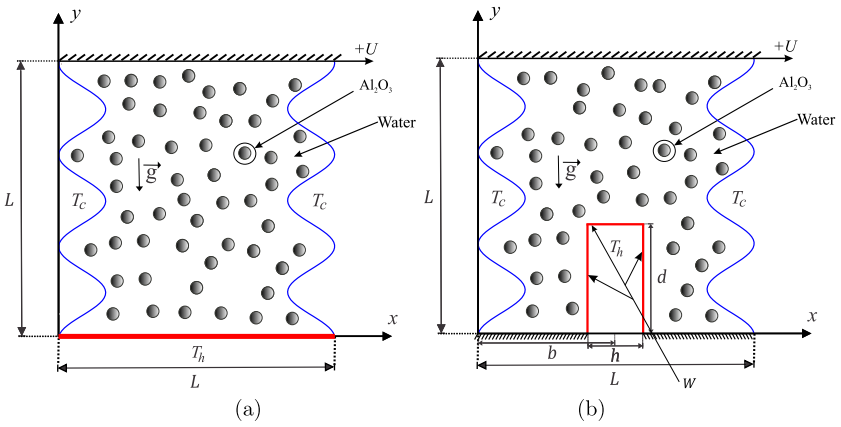

Fig. 1. Schematic design of the physical model for (a) Case 1 and (b) Case 2.

1. Introduction

Research on identifying effective methods to improve the heat transfer processes and reduce energy losses inside thermal energy systems is still ongoing in order to evaluate the performance and efficiency of such systems. So far, numerous engineering applications have been developed for thermal convection inside nanofluid-filled enclosures. Heating and cooling thermal devices, solar power thermal applications, industrial thermal exchangers, refrigeration techniques, storage technologies, etc., are examples of the use of nanofluids in both natural and mixed convection applications [1–8]. Several scientific papers have so far been published concerning the thermal convection of nanofluids-filled enclosures [9–18]. By way of illustration, the features of mixed convection flow under the influence of magnetic forces inside a lid-driven domain having a hot corrugated surface have been explored by Sheikholeslami and Chamkha [19]. They realised that the overall heat transfer did augment with the growth of the value of the Reynolds number, nanoparticles' concentration in volume, and magnetic number, while the Hartmann number was seen to have negative influences. Oztop et al. [20] evaluated magnetic-mixed convection within a lid-driven domain heated from the corner. Some interesting results have been reported. Rashad et al. [21] elaborated a numerical code to examine the magnetic-natural convective nanoliquid behavior and production of entropy within an inclined porous enclosure. The findings describe the influences of the following parameters: volume fraction, Hartmann number, Rayleigh number, heat generation/absorption parameter, and emplacement of the heat/sink source. Alsabery et al. [22] have employed simulation codes to modulate the thermal-natural convection of a nanofluid flowing in undulated enclosures based on the local thermal non-equilibrium (LTNE) approach in porous media. The nanoparticles' volume fraction and the magnetic field have been found to adversely affect the thermal convection inside the porous enclosure. Sheikholeslami [23] He explained the magnetic field force on the heat transfer within a porous medium of nanoliquid filled-waved-circular enclosure under the non-Darcy model. The findings revealed that the rate of heat transfer occurred reducing through the rising of Rayleigh number and decreasing magnetic forces. Dogonchi et al. [24] elaborated a CVFEM-based simulation code to explore magnetic-thermal-free convection of nanoliquid flow in a porous annulus considering Brownian motions.

Nevertheless, it has become desirable to adopt the two-phase nanofluid approach including the effects of thermophoresis and Brownian motions to simulate natural convection in nanofluids as it has been found to be more accurate [25–28]. In the experimental investigation of Wen and Ding [26], it was stated that the migration of γ-Al_2O_3 nanoparticles within the entrance area of a tube flow may be attributed to Brownian motions, shear effects and viscosity gradients. Hashim et al. [29] carried out a computational analysis using a FEM-based numerical code to analyze thermal-free convection in an undulated enclosure loaded with Al_2O_3-water mixture employing two-phase nanofluid technique. Alsabery et al. [30] examined the thermal-forced convection within a lid-driven enclosure including a heated triangular surface. In this regard, they adopted the two-phase nanoliquid form. The outcomes prove that the increasing of Hartmann number reaches to an increased in the Brownian motion, which increases the migration of the solid particles. Numerical study of forced convection heat transfer process and irreversibility characteristic into a lid-driven cavity including two rotating cylinders loaded with a nanoliquid within the presence of a magnetic field is performed by Barnoon et al. [31]. They have utilized a two-phase technique for simulating the fluid flow and heat transfer in nanoliquids. The researchers noted that with a decrease in Hartmann and Richardson numbers as well as an improvement into the nanoparticle concentration, the rate of heat transfer would increase. Garmroodi et al. [32] simulated MHD-thermal forced convection inside a cavity having double rotating cylinders in various forms. In this regard, a two-phase pattern was employed to analyze the convection heat transfer of the applied nanoliquid. The improvement within the Hartmann number has been found to result in a reduction into the heat transfer rate, and the maximal impact of the magnetic field occurs toward the vertical alignment of two rotating cylinders. Sheremet and Pop [33] analysed thermal-mixed convection within a nanofluid filled-lid-driven container. The investigation is numerical which is accomplished by solving the governing equations, including Buongiorno's mathematical model, with the numerical technique of finite difference method. The two-phase approach was used to numerically analyze the thermal-free convection problem of nanofluid-filled square domain in the study of Esfandiary et al. [34] and Motlagh and Soltanipour [35]. The study results showed that the thermal transmission rate inside the cavity improved midst the rising nanoparticles' concentration up to 4%. In the study of Alsabery et al. [36], the influence of the

non-homogeneous (two-phase) nanofluid approach at magneto-thermal-mixed convection inside a double lid-driven was addressed. Thermophoresis diffusion and Brownian motions have been found to present an outstanding task in developing thermal-convective transfer. Izadi et al. [37,38] have applied the two-phase nanofluid technique in the porous media to study natural and forced convection characteristics of nanofluids.

The key objective of this analysis is to discuss mixed convective flow characteristics and heat transfer behavior inside a complex-wavy-walled container. The cavity is assumed to be saturated by alumina-water nanofluid. The two-phase nanofluid approach is utilized. The finite element technique is employed during the numerical solutions. Results have been represented with isolines of temperature, stream function, and concentration of nanoparticles, as well as with graphs of Nusselt numbers and local nanoparticles' distribution variations versus the examined parameters.

2. Mathematical formulation

Mixed convective flow and heat transfer mechanism within the wavy-walled container with length L and having a heat source at the bottom with height d and width h, as outlined in Fig. 1(a) and (b). A prominent source (isothermal) heater with length and width of d and h is kept at a determined hot temperature (T_h). The wavy surfaces of the container are held at a cold temperature (T_c). The top moving surface and bottom surface are insulated. All of the container surfaces are considered to be impermeable surfaces with no-slip conditions, and the nanoliquid within the wavy container is Al_2O_3-water which is incompressible Newtonian fluid and the flow is steady.

Based on the Boussinesq approximation, the continuity, momentum and energy equations concerning the laminar and steady convection are presented as [29,39]:

$$\nabla \cdot \mathbf{v} = 0, \tag{1}$$

$$\rho_{nf}\mathbf{v}\cdot\nabla\mathbf{v} = -\nabla p + \nabla\cdot(\mu_{nf}\nabla\mathbf{v}) + (\rho\beta)_{nf}(T-T_c)\vec{g}, \tag{2}$$

$$(\rho C_p)_{nf}\mathbf{v}\cdot\nabla T = \nabla\cdot(k_{nf}\nabla T) - C_{p,p}J_p\cdot\nabla T, \tag{3}$$

$$\mathbf{v}\cdot\nabla\varphi = -\frac{1}{\rho_p}\nabla\cdot J_p, \tag{4}$$

$\mathbf{v}$, $\vec{g}$ and φ are the velocity vector, gravitational acceleration vector and the local volume fraction of nanoparticles and J_p shows the nanoparticles mass flux which is addressed as:

$$J_p = J_{p,B} + J_{p,T}, \tag{5}$$

$$J_{p,B} = -\rho_p D_B \nabla\varphi, \quad D_B = \frac{k_b T}{3\pi\mu_f d_p}, \tag{6}$$

$$J_{p,T} = -\rho_p D_T \frac{\nabla T}{T}, \quad D_T = 0.26\frac{k_f}{2k_f+k_p}\frac{\mu_f}{\rho_f T}\varphi. \tag{7}$$

The features of the employed nanofluid in this research are as follows [39]:

$$(\rho C_p)_{nf} = (1-\varphi)(\rho C_p)_f + \varphi(\rho C_p)_p, \tag{8}$$

$$\alpha_{nf} = \frac{k_{nf}}{(\rho C_p)_{nf}}, \tag{9}$$

$$\rho_{nf} = (1-\varphi)\rho_f + \varphi\rho_p, \tag{10}$$

$$(\rho\beta)_{nf} = (1-\varphi)(\rho\beta)_f + \varphi(\rho\beta)_p. \tag{11}$$

$$\frac{\mu_{nf}}{\mu_f} = \frac{1}{1-34.87\left(\frac{d_p}{d_f}\right)^{-0.3}\varphi^{1.03}}, \tag{12}$$

$$\frac{k_{nf}}{k_f} = 1 + 4.4\mathrm{Re}_B^{0.4}\mathrm{Pr}^{0.66}\left(\frac{T}{T_{fr}}\right)^{10}\left(\frac{k_p}{k_f}\right)^{0.03}\varphi^{0.66}, \tag{13}$$

here Re_B is determined as:

$$\mathrm{Re}_B = \frac{\rho_f u_B d_p}{\mu_f}, \quad u_B = \frac{2k_b T}{\pi\mu_f d_p^2}. \tag{14}$$

The molecular diameter of the applied liquid (water)d_f is given as [39]:

$$d_f = 0.1\left[\frac{6M}{N^*\pi\rho_f}\right]^{\frac{1}{3}}. \tag{15}$$

The following non-dimensional variables are employed:

$$\begin{aligned} &X = \frac{x}{L},\ Y = \frac{y}{L},\ \mathbf{V} = \frac{\mathbf{v}}{U_0},\ P = \frac{pL^2}{\rho_{nf}\nu_f^2},\ \varphi^* = \frac{\varphi}{\varphi},\ D_B^* = \frac{D_B}{D_{B0}},\\ &D_T^* = \frac{D_T}{D_{T0}},\ \delta = \frac{T_h - T_c}{T_c},\ \theta = \frac{T - T_c}{T_h - T_c},\ (D,H,B) = \frac{(d,h,b)}{L}. \end{aligned} \tag{16}$$

Hence, (1)–(4) are made dimensionless

$$\nabla\cdot\mathbf{V} = 0, \tag{17}$$

$$\mathbf{V}\cdot\nabla\mathbf{V} = -\frac{1}{Re^2}\nabla P + \frac{\rho_f}{\rho_{nf}}\frac{\mu_{nf}}{\mu_f}\frac{1}{Re}\nabla^2\mathbf{V} + \frac{(\rho\beta)_{nf}}{\rho_{nf}\beta_f}Ri\,\theta, \tag{18}$$

$$\begin{aligned} \mathbf{V}\cdot\nabla\theta = {}& \frac{(\rho C_p)_f}{(\rho C_p)_{nf}}\frac{k_{nf}}{k_f}\frac{1}{Re\cdot\Pr}\nabla^2\theta + \frac{(\rho C_p)_f}{(\rho C_p)_{nf}}\frac{D_B^*}{Re\cdot\Pr\cdot Le}\nabla\varphi^*\cdot\nabla\theta\\ &+\frac{(\rho C_p)_f}{(\rho C_p)_{nf}}\frac{D_T^*}{Re\cdot\Pr\cdot Le\cdot N_{BT}}\frac{\nabla\theta\cdot\nabla\theta}{1+\delta\theta}, \end{aligned} \tag{19}$$

$$\mathbf{V}\cdot\nabla\varphi^* = \frac{D_B^*}{Re\cdot Sc}\nabla^2\varphi^* + \frac{D_T^*}{Re\cdot Sc\cdot N_{BT}}\cdot\frac{\nabla^2\theta}{1+\delta\theta}, \tag{20}$$

where

$$\begin{aligned} &\mathbf{V} = (U_0, V_0),\ D_{T0} = 0.26\frac{k_f}{2k_f + k_p}\frac{\mu_f}{\rho_f T_c}\varphi,\ D_{B0} = \frac{k_b T_c}{3\pi\mu_f d_p},\\ &Sc = \frac{\nu_f}{D_{B0}},\ N_{BT} = \frac{\varphi D_{B0}T_c}{D_{T0}(T_h - T_c)},\ Le = \frac{k_f}{(\rho C_p)_f\varphi D_{B0}},\\ &Ri = \frac{Gr}{Re^2},\ Gr = \frac{g\rho_f\beta_f(T_h - T_c)L^3}{\nu_f^2},\ \Pr = \frac{\nu_f}{\alpha_f}. \end{aligned} \tag{21}$$

The full derivation of the above mentioned system of equations is presented in the Appendix section. Accordingly, the boundary conditions are:

$$\text{Top wall: } U = 1,\ V = 0,\ \frac{\partial\varphi^*}{\partial n} = 0,\ \frac{\partial\theta}{\partial n} = 0, \tag{22}$$

$$\begin{aligned} &\text{Heat source}\left(Y = D,\ \frac{1-H}{2} \le X \le \frac{1+H}{2}\right):\\ &\quad U = V = 0,\ \frac{\partial\varphi^*}{\partial n} = -\frac{D_T^*}{D_B^*}\cdot\frac{1}{N_{BT}}\cdot\frac{1}{1+\delta\theta}\frac{\partial\theta}{\partial n},\ \theta = 1, \end{aligned} \tag{23}$$

$$\begin{aligned} &\text{Bottom wall}\left(0 \le X \le \frac{1-H}{2}, \frac{1+H}{2} \le X \le 1\right):\\ &\quad U = V = 0,\ \frac{\partial\varphi^*}{\partial n} = 0,\ \frac{\partial\theta}{\partial n} = 0, \end{aligned} \tag{24}$$

$$\begin{aligned} &\text{Left wall } (1 - A[1 - \cos(2N\pi X)],\ 0 \le Y \le 1):\\ &\quad U = V = 0,\ \frac{\partial\varphi^*}{\partial n} = -\frac{D_T^*}{D_B^*}\cdot\frac{1}{N_{BT}}\cdot\frac{1}{1+\delta\theta}\frac{\partial\theta}{\partial n},\ \theta = 0, \end{aligned} \tag{25}$$

$$\begin{aligned} &\text{Rigth wall } [A(1 - \cos(2N\pi X)],\ 0 \le Y \le 1):\\ &\quad U = V = 0,\ \frac{\partial\varphi^*}{\partial n} = -\frac{D_T^*}{D_B^*}\cdot\frac{1}{N_{BT}}\cdot\frac{1}{1+\delta\theta}\frac{\partial\theta}{\partial n},\ \theta = 0. \end{aligned} \tag{26}$$

At the heated part of the lower wall, we can calculate the local Nusselt number (Nu_{nf})

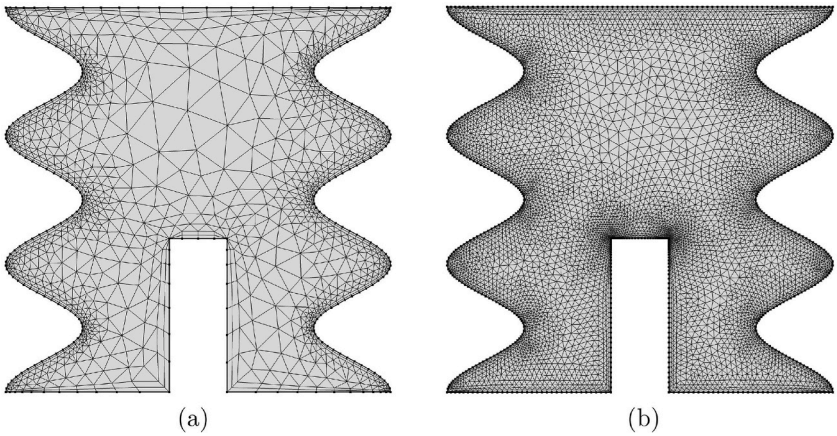

Fig. 2. (a) 2487 elements and (b) 13444 elements.

Table 1
Grid sensitivity checks of $\overline{Nu}$ for $Ri = 1$, Re $= 100$, $\varphi = 0.02$, $N = 3$, $A = 0.1$, $D = 0.4$ and $H = 0.2$.

Size of grid	Number of elements	$\overline{Nu}$
G1	3636	144.73
G2	5409	147.64
G3	13444	149.95
G4	28644	151.63
G5	59920	151.63

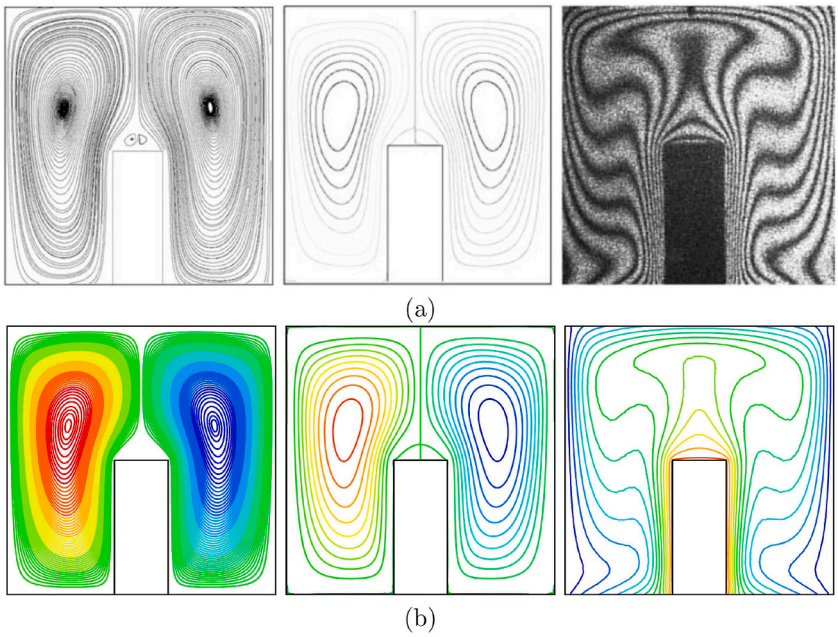

Fig. 3. (a) Paroncini and Corvaro [40] and (b) present work [experimental streamlines (left), numerical streamlines (middle) and experimental isotherms (right) for $Ra = 1.78 \times 10^5$, Pr $= 0.71$, $A = 0$, $D = 0.5$, $\varphi = 0$].

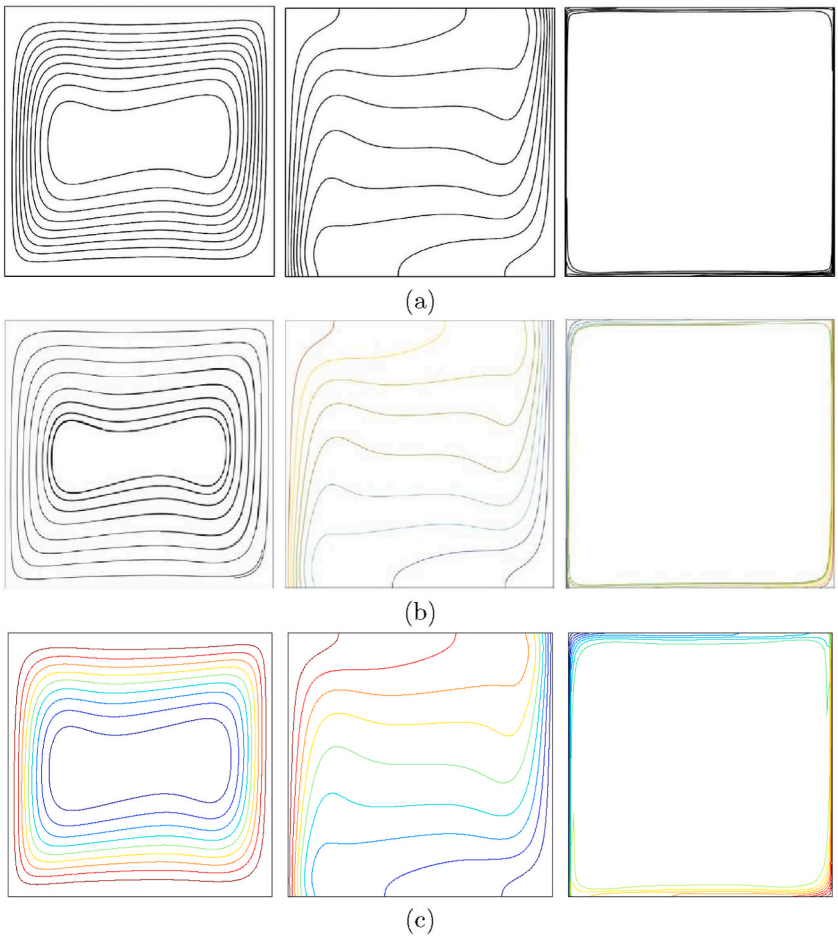

Fig. 4. (a) Corcione et al. [41], (b) Wang et al. [42] and (c) current investigation [streamlines (left), isotherms (middle), and nanoparticle distribution (right) for $Ra = 3.37 \times 10^5$, $\varphi = 0.04$, $N = 0$, $D = 0$].

Table 2
Ranges of the used parameters values.

Parameter	Range
φ	0.00, 0.01, 0.02, 0.03
Aspect Ratio $(AR = \frac{D}{H})$	0.5, 1, 2
N	1, 3, 5
A	0.05, 0.10, 0.15

$$Nu = -\frac{k_{nf}}{k_f}\left(\frac{\partial\theta}{\partial W}\right)_W. \tag{27}$$

where W performs the entire portion of the active source. The average heat transfer (Nusselt number) evaluated on the heated source is

$$\overline{Nu} = \int_0^W Nu_{nf}\mathrm{d}W. \tag{28}$$

3. Solution approach

The system of equations of interest is as given in (17)–(20) subject to (22)–(26). The Galerkin weighted residual FEM is employed to solve the system. The details of the procedure are described as follows:

1. First, the penalty FEM employed to exclude the pressure (P) by adding the penalty parameter (λ) as the following:

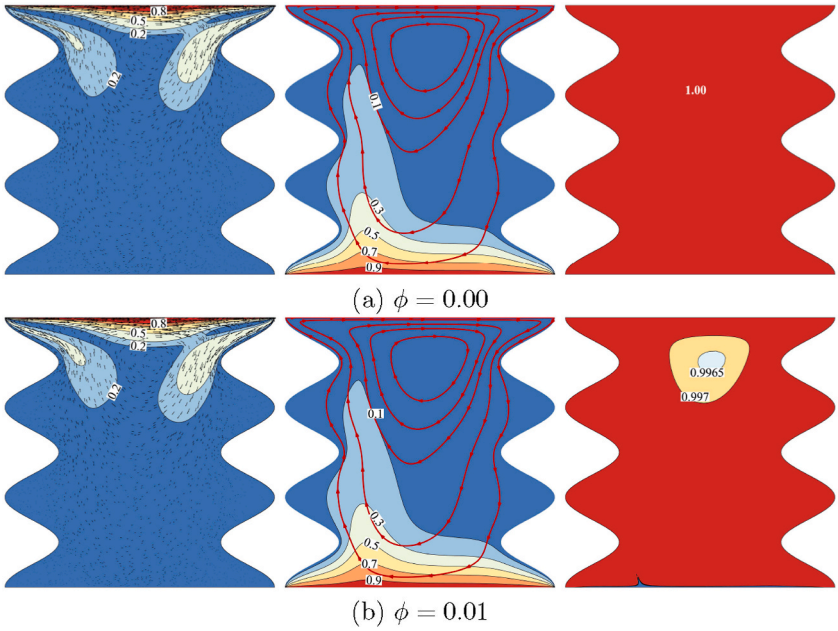

Fig. 5. (left) Velocity magnitude contour and velocity vectors, (middle) Isotherms and streamlines contours, (right) Concentration contours rise by solid volume fraction ($\varphi = 0.00$ and $\varphi = 0.01$) for case 1, $Ri = 1$, $A = 0.1$ and $N = 3$.

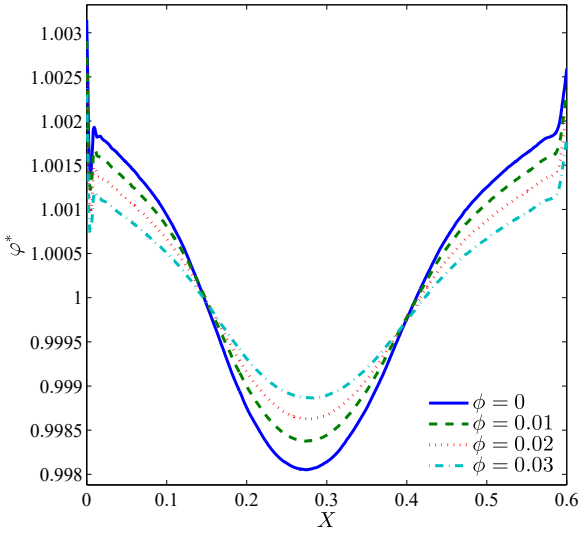

Fig. 6. φ^* vs. X for several φ along $Y = 0.5$ (Case 1, $Ri = 1$, $A = 0.1$, $N = 3$).

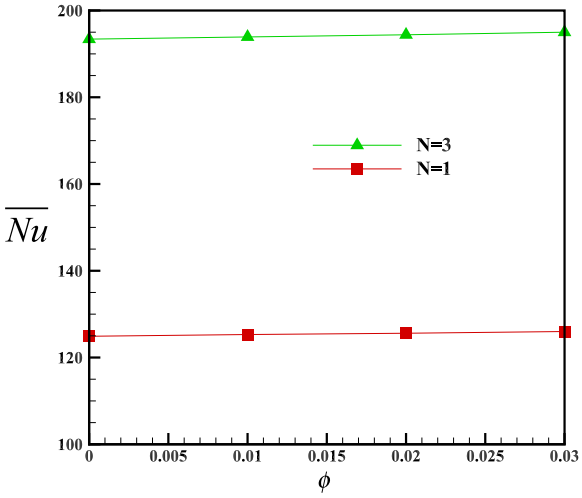

Fig. 7. $\overline{Nu}$ vs. φ for several N (Case 1, $Ri = 1$, $A = 0.1$).

$$P = -\lambda\left(\frac{\partial U}{\partial X} + \frac{\partial V}{\partial Y}\right),$$

where it reaches into the next momentum equations via X and Y-directions:

$$\begin{aligned} U\frac{\partial U}{\partial X} + V\frac{\partial U}{\partial Y} &= \frac{1}{Re^2}\frac{\partial \lambda}{\partial X}\left(\frac{\partial U}{\partial X} + \frac{\partial V}{\partial Y}\right) + \frac{\rho_f}{\rho_{nf}}\frac{\mu_{nf}}{\mu_f}\frac{1}{Re}\left(\frac{\partial^2 U}{\partial X^2} + \frac{\partial^2 U}{\partial Y^2}\right), \\ U\frac{\partial V}{\partial X} + V\frac{\partial V}{\partial Y} &= \frac{1}{Re^2}\frac{\partial \lambda}{\partial Y}\left(\frac{\partial U}{\partial X} + \frac{\partial V}{\partial Y}\right) + \frac{\rho_f}{\rho_{nf}}\frac{\mu_{nf}}{\mu_f}\frac{1}{Re}\left(\frac{\partial^2 V}{\partial X^2} + \frac{\partial^2 V}{\partial Y^2}\right) \\ &\quad + \frac{(\rho\beta)_{nf}}{\rho_{nf}\beta_f} Ri\,\theta. \end{aligned}$$

2. The resulting weak formulations are achieved through multiplying the momentum equations with an interior region (Φ) and integrating the result over the computational domain which is discretised toward small triangular components as shown in Fig. 2.

$$\begin{aligned} &\int_\Omega \left(\Phi_i U^k \frac{\partial U^k}{\partial X} + \Phi_i V^k \frac{\partial U^k}{\partial Y}\right) dX dY = \frac{\lambda}{Re^2}\int_\Omega \frac{\partial \Phi_i}{\partial X}\left(\frac{\partial U^k}{\partial X} + \frac{\partial V^k}{\partial Y}\right) dX dY \\ &\quad + \frac{\rho_f}{\rho_{nf}}\frac{\mu_{nf}}{\mu_f}\frac{1}{Re}\int_\Omega \Phi_i\left(\frac{\partial^2 U^k}{\partial X^2} + \frac{\partial^2 U^k}{\partial Y^2}\right) dX dY, \\ &\int_\Omega \left(\Phi_i U^k \frac{\partial V^k}{\partial X} + \Phi_i V^k \frac{\partial V^k}{\partial Y}\right) dX dY = \frac{\lambda}{Re^2}\int_\Omega \frac{\partial \Phi_i}{\partial Y}\left(\frac{\partial U^k}{\partial X} + \frac{\partial V^k}{\partial Y}\right) dX dY \\ &\quad + \frac{\rho_f}{\rho_{nf}}\frac{\mu_{nf}}{\mu_f}\frac{1}{Re}\int_\Omega \Phi_i\left(\frac{\partial^2 V^k}{\partial X^2} + \frac{\partial^2 V^k}{\partial Y^2}\right) dX dY + \frac{(\rho\beta)_{nf}}{\rho_{nf}\beta_f} Ri \int_\Omega \Phi_i \theta_{nf}^k dX dY. \end{aligned}$$

3. Use the interpolation functions to approximate the velocity pattern and temperature distributions as:

$$U \approx \sum_{j=1}^{m} U_j \Phi_j(X,Y), \quad V \approx \sum_{j=1}^{m} V_j \Phi_j(X,Y), \quad \theta \approx \sum_{j=1}^{m} \theta_j \Phi_j(X,Y).$$

4. The nonlinear residual equations associated with the momentum equations are:

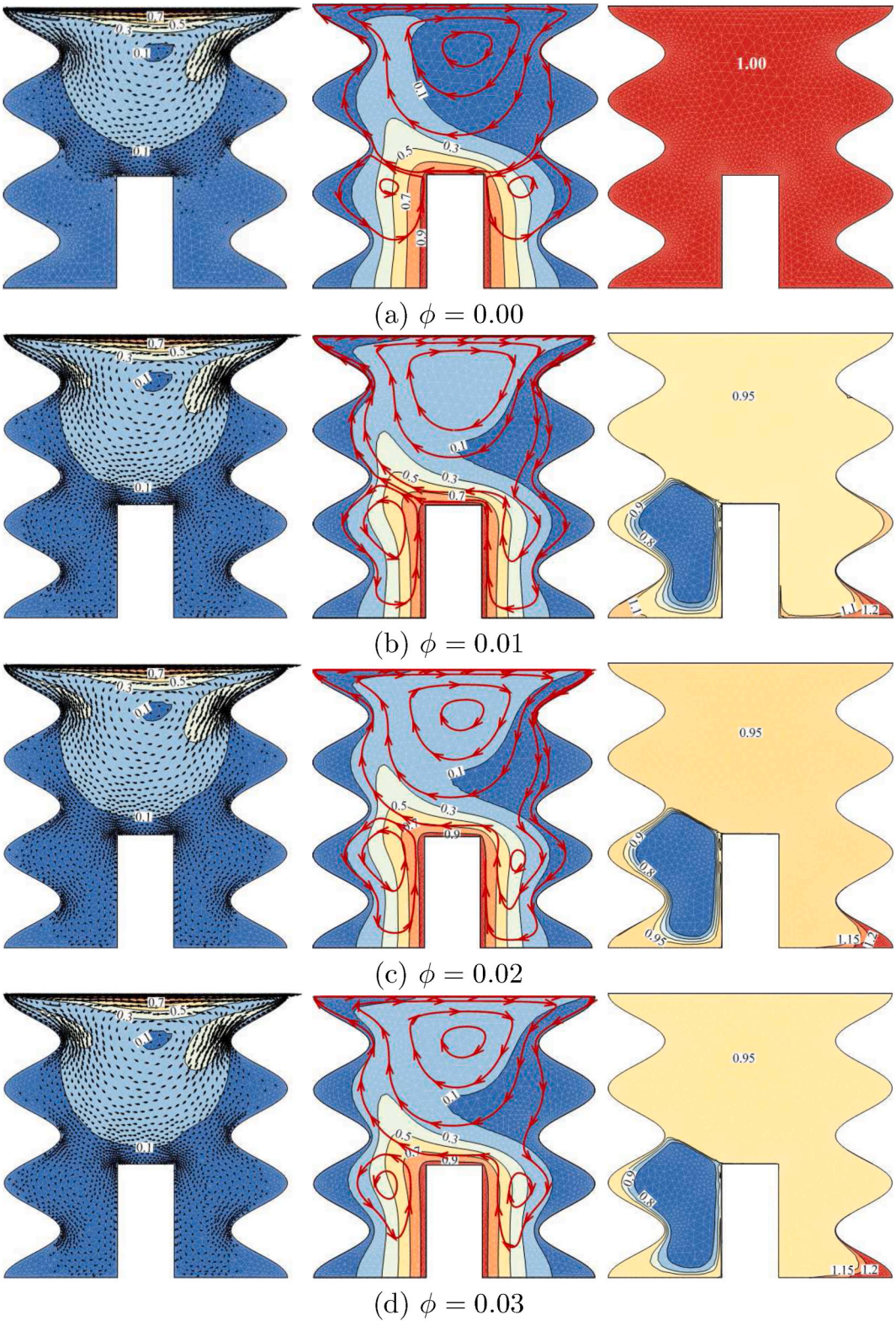

Fig. 8. (left) Velocity magnitude contour and velocity vectors, (middle) Isotherms and streamlines contours, (right) Concentration contours rise by solid volume fraction (φ) for case 2, $Ri = 1$, $A = 0.1$, $N = 3$ and $AR = 2$.

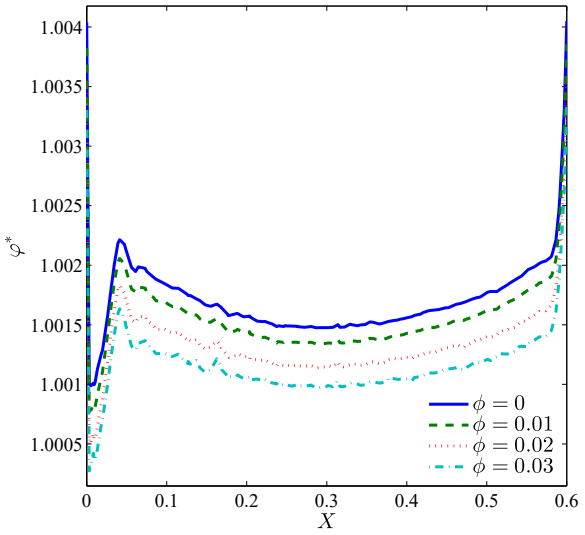

Fig. 9. φ^* vs. X for several φ along $Y = 0.5$ (Case 2, $Ri = 1$, $A = 0.1$, $N = 3$, $AR = 2$).

$$
\begin{aligned}
R(1)_i &= \sum_{j=1}^{m} U_j \int_{\Omega} \left[\left(\sum_{j=1}^{m} U_j \Phi_j \right) \frac{\partial \Phi_j}{\partial X} + \left(\sum_{j=1}^{m} V_j \Phi_j \right) \frac{\partial \Phi_j}{\partial Y} \right] \Phi_i \mathrm{d}X\mathrm{d}Y \\
&\quad + \frac{\lambda}{Re^2} \left[\sum_{j=1}^{m} U_j \int_{\Omega} \frac{\partial \Phi_i}{\partial X} \frac{\partial \Phi_j}{\partial X} \mathrm{d}X\mathrm{d}Y + \sum_{j=1}^{m} V_j \int_{\Omega} \frac{\partial \Phi_i}{\partial X} \frac{\partial \Phi_j}{\partial Y} \mathrm{d}X\mathrm{d}Y \right] \\
&\quad + \frac{\rho_f}{\rho_{nf}} \frac{\mu_{nf}}{\mu_f} \frac{1}{Re} \sum_{j=1}^{m} U_j \int_{\Omega} \left[\frac{\partial \Phi_i}{\partial X} \frac{\partial \Phi_j}{\partial X} + \frac{\partial \Phi_i}{\partial Y} \frac{\partial \Phi_j}{\partial Y} \right] \mathrm{d}X\mathrm{d}Y, \\
R(2)_i &= \sum_{j=1}^{m} V_j \int_{\Omega} \left[\left(\sum_{j=1}^{m} U_j \Phi_j \right) \frac{\partial \Phi_j}{\partial X} + \left(\sum_{j=1}^{m} V_j \Phi_j \right) \frac{\partial \Phi_j}{\partial Y} \right] \Phi_i \mathrm{d}X\mathrm{d}Y \\
&\quad + \frac{\lambda}{Re^2} \left[\sum_{j=1}^{m} U_j \int_{\Omega} \frac{\partial \Phi_i}{\partial Y} \frac{\partial \Phi_j}{\partial X} \mathrm{d}X\mathrm{d}Y + \sum_{j=1}^{m} V_j \int_{\Omega} \frac{\partial \Phi_i}{\partial Y} \frac{\partial \Phi_j}{\partial Y} \mathrm{d}X\mathrm{d}Y \right] \\
&\quad + \frac{\rho_f}{\rho_{nf}} \frac{\mu_{nf}}{\mu_f} \frac{1}{Re} \sum_{j=1}^{m} V_j \int_{\Omega} \left[\frac{\partial \Phi_i}{\partial X} \frac{\partial \Phi_j}{\partial X} + \frac{\partial \Phi_i}{\partial Y} \frac{\partial \Phi_j}{\partial Y} \right] \mathrm{d}X\mathrm{d}Y.
\end{aligned}
$$

5. To simplify the nonlinear terms in the momentum equations, the Newton-Raphson iteration algorithm is used:

$$\Gamma^{m+1} = \Gamma^m - [f'(\Gamma^m)]^{-1} f(\Gamma^m).$$

6. Convergence of the solution is achieved by the following convergence criteria:

$$\left\| \frac{\Gamma^{m+1} - \Gamma^m}{\Gamma^{m+1}} \right\| \leq \varepsilon.$$

Toward assuring the existing numerical system's confidence at the numerical domain's grid size, we have adopted various grid sizes and determined the average Nusselt number regarding $N = 3$, $Ra = 10^5 \varphi = 0.02$, $H = 0.5$ and $D = 0.3$. Such a scheme is displayed in Table 1 that designate insignificant changes via the G4 grids and exceeding. Therefore, for all calculations within this investigation, the G4 uniform grid does implement.

To validate the present approach, we consider convection in a square enclosure having a heated rectangle placed at the bottom wall. In Fig. 3 we show the numerical data of the present work and Paroncini and Corvaro [40]'s experimental and numerical results. Moreover, the two-phase nanofluid model is verified by comparisons in Fig. 4 for the numerical outputs of Corcione et al. [41] and Wang et al. [42]. The outcomes of the above validations are provided apparent confidence in the current design and simulations' correctness.

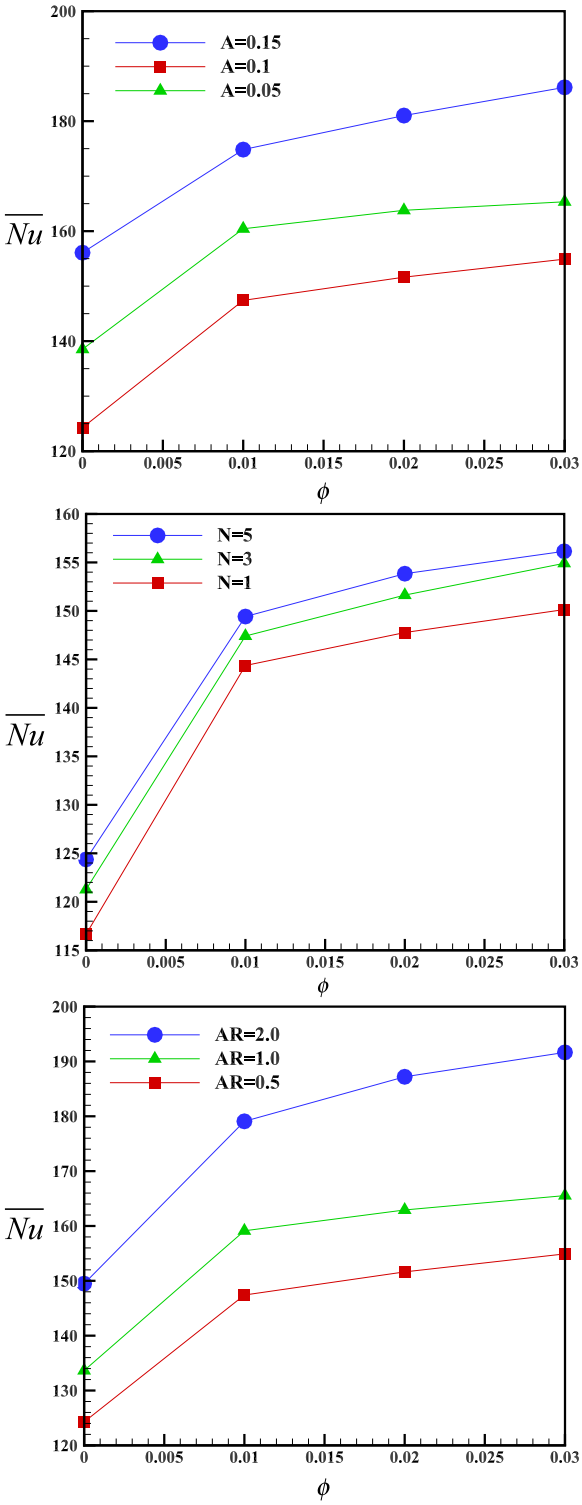

Fig. 10. $\overline{Nu}$ vs. φ for various (top) A at $N = 3$, $AR = 2$, (middle) N at $A = 0.1$, $AR = 2$, and (bottom) AR at $A = 0.1$, $N = 3$ (Case 2, $Ri = 1$).

4. Results and discussion

In the current section, the numerical solution outcomes, consisting of contours of velocity magnitude and velocity vectors, temperature isolines, streamlines and Al_2O_3 nanoparticles' concentration, and graphs of local normalized solid volume fraction and mean

Nusselt number for various Ri, N, A, AR, and φ with various ranges as shown in Table 2 for the two considered configuration cases are presented. The other parameters are fixed at $\mathrm{Pr} = 4.623$, $Le = 3.5 \times 10^5$, $Sc = 3.55 \times 10^4$, $N_{BT} = 1.1$ and $\delta = 155$.

Fig. 5 displays from left to right, respectively: velocity magnitude and velocity vectors contours, isotherms and streamlines fields, and nanoparticles' concentration for case 1 at $\varphi = 0.00$ and $\varphi = 0.01$ when $Ri = 1$, $A = 0.1$ and $N = 3$. For this first geometrical configuration, the streamlines flow patterns indicate that the flow mechanism is principally characterized by the presence of a large clockwise-rotating vortex. In fact, the hot bottom wall heated the surrounding fluid, causing its density layers to decrease, and the fluid particles thus move upwardly. Near the cold sidewalls, the same behavior occurs in the opposite direction. The moving upper wall of the cavity helps the fluid to rotate clockwise, under the shear-driven effects, and the thermal panache to develop upward on the left side as shown isotherms contours. The values of fluid velocity are observed to be large nearest the moving upper wall owing to the shear effect forces. It is apparent that due to the centrifugal forces that drive away the nanoparticles (because of the slip velocity between the nanoparticles and the base fluid), the nanoparticles' distribution portrays minimum concentrations within the flow vortex core. Also, near the hot bottom wall, we notice minimum concentrations of nanoparticles due to the thermophoretic diffusion forces. This is because the nanoparticles gained higher kinetic energy from the bottom wall. It is noteworthy that according to equation (20), solving the concentration equation for zero concentration is not applicable and it should be solved directly.

Fig. 6 aims to preview the distribution from nanoparticles along the line $Y = 0.5$ in the X-direction for Case 1. An extreme variation of particles' concentration near the cold sides walls can be noticed. The large degree of nanoparticles' concentration could be observed at both cold surfaces. That occurs because of the thermophoresis effects, which tend to transfer the nanoparticles from heated regions to cold regions. In the middle of the cavity, the concentration of nanoparticles remains insignificant due to the circulation zone.

The objective of Fig. 7 is to show the role of the number of undulations (N) on the mean heat transport. It is clear that increase the number of undulations augments the mean Nusselt number. This is mainly due to an increase in the exchange surfaces within the cavity. For this case, a small effect of the addition of nanoparticles on the mean Nusselt number was found.

Fig. 8 shows contours of velocity magnitude, isotherms, streamlines, and nanoparticles' concentration with the respect of solid volume fraction (φ) for Case 2 under the same studied parameters: $Ri = 1$, $A = 0.1$, $N = 3$ and $AR = 2$. The heater on the bottom wall has the effect of changing the flow configuration as two secondary flow vortices are detached from the main vortex. The vortex on the right of the prominent heater merges with the main vortex with a rise of the value of φ. The circulation zones push the nanoparticles to agglomerate near the sidewalls of the enclosure, especially at the bottom part.

The variations of the local normalized solid volume fraction φ^* with X for several φ along $Y = 0.5$ in the X-direction are graphically represented in Fig. 9. It can be concluded that the nanoparticles in the cavity have a homogeneous distribution, except near the wavy sidewalls, which are found to be strongly localized.

Fig. 10(top) and 10 (middle) aim to examine the role of the volume fraction, undulation number, and undulation amplitude on the overall heat transfer rate for Case 2. It is clear that the value of average Nu increases by the growth of φ for the same values of N and A. Also, the heat transfer rate increases with increasing N for the same values of φ and A. The most important amount of heat transfer rate is achieved for the higher amplitude of undulations, $A = 0.15$. Fig. 10(bottom) characterizes the average Nu toward the heated source cavity with different volume fraction values, φ and aspect ratio of the heat source, AR of case 2 for the studied parameters: $Ri = 1$, $A = 0.1$ and $N = 3$. It is apparent that the value of Nu rises with an improvement in AR for the same amount of φ.

5. Conclusions

In this contribution, the free convection of alumina-water nanoliquid within 2D wavy-walled container heated from below with or without a prominent heater situated on the bottom surface of the container did examine. The nanofluid two-phase form has been applied. The critical observations expressed of the existing research are given during the following:

1. The existence of a prominent heater situated at the bottom of the cavity holds an essential impact on flow structure, nanoparticles' distributions, and convective heat transfer rate.
2. It remains evident that increase the number of undulations augments the mean Nusselt number for both geometrical configurations.
3. A high degree of nanoparticles' concentration was observed at both cold side surfaces due to the thermophoresis diffusion effects.
4. The convective heat transfer rate was observed to be best toward the maximum values of N and φ for case 1, and maximum values of N, A, φ and AR for Case 2.
5. The influence regarding volume fraction of nanoparticles was found to occur more noticeable for case 2.

Declaration of competing interest

The authors declare that they have no known competing financial interests or personal relationships that could have appeared to influence the work reported in this paper.

Acknowledgments

The work was supported by the Universiti Kebangsaan Malaysia (UKM) research grant GP-2021-K006388. We thank the respected reviewers for their constructive comments which clearly enhanced the quality of the manuscript.

Appendix

First, all independent parameters are modified into the non-dimensional form according to

$$X=\frac{x}{L},\ \ Y=\frac{y}{L},\ \ \mathbf{V}=\frac{\mathbf{v}}{U_0},\ \ P=\frac{pL^2}{\rho_{nf}\nu_f^2},\ \ \varphi^*=\frac{\varphi}{\varphi},$$
$$D_B^*=\frac{D_B}{D_{B0}},\ \ D_T^*=\frac{D_T}{D_{T0}},\ \ \delta=\frac{T_h-T_c}{T_c},\ \ \theta=\frac{T-T_c}{T_h-T_c}. \tag{29}$$

Transforming the continuity equation into its non-dimensional form leads to the following:

$$\nabla\cdot\mathbf{v}=\frac{\partial u}{\partial x}+\frac{\partial v}{\partial y}=\frac{\partial UU_0}{\partial XL}+\frac{\partial VU_0}{\partial YL}=U_0\frac{\nabla}{L}\cdot\mathbf{V}=0\ \Rightarrow\ \nabla\cdot\mathbf{V}=0. \tag{30}$$

The dimensionless momentum equation is obtained as follows:

$$\rho_{nf}\mathbf{v}\cdot\nabla\mathbf{v}=-\nabla p+\nabla\cdot(\mu_{nf}\nabla\mathbf{v})+(\rho\beta)_{nf}(T-T_c)\overrightarrow{g}, \tag{31}$$

$$\rho_{nf}\mathbf{V}U_0\frac{\nabla}{L}\mathbf{V}U_0=-\frac{\nabla}{L}\frac{P\rho_{nf}\nu_f^2}{L^2}+\frac{\nabla}{L}\cdot\left(\mu_{nf}\frac{\nabla}{L}\mathbf{V}U_0\right)+(\rho\beta)_{nf}\theta(T_h-T_c)\overrightarrow{g}, \tag{32}$$

$$\frac{L}{\rho_{nf}U_0^2}\times\left[\rho_{nf}\mathbf{V}U_0\frac{\nabla}{L}\mathbf{V}U_0=-\frac{\nabla}{L}\frac{P\rho_{nf}\nu_f^2}{L^2}+\frac{\nabla}{L}\cdot\left(\mu_{nf}\frac{\nabla}{L}\mathbf{V}U_0\right)+(\rho\beta)_{nf}\theta(T_h-T_c)\overrightarrow{g}\right], \tag{33}$$

$$\mathbf{V}\cdot\nabla\mathbf{V}=-\underbrace{\frac{\nu_f^2}{U_0^2L^2}}_{\frac{1}{\mathrm{Re}^2}}\nabla P+\underbrace{\frac{\nu_{nf}}{U_0L}}_{\frac{\nu_{nf}}{\nu_f}\frac{1}{\mathrm{Re}}}\nabla\cdot\nabla\mathbf{V}+\underbrace{\frac{L\beta_{nf}}{U_0^2}(T_h-T_c)\overrightarrow{g}\,\theta}_{\frac{\beta_{nf}}{\beta_f}\frac{L\beta_f}{U_0^2}(T_h-T_c)\overrightarrow{g}=\frac{\beta_{nf}}{\beta_f}Ri}, \tag{34}$$

$$\mathbf{V}\cdot\nabla\mathbf{V}=-\frac{1}{\mathrm{Re}^2}\nabla P+\frac{\rho_f}{\rho_{nf}}\frac{\mu_{nf}}{\mu_f}\frac{1}{\mathrm{Re}}\nabla^2\mathbf{V}+\frac{\beta_{nf}}{\beta_f}Ri\,\theta. \tag{35}$$

J_p consists of two part as explained in relation (36) which by defining non-dimensional parameters in (37) it would be defined as relation (38).

$$J_p=J_{p,B}+J_{p,T}=-\rho_pD_B\nabla\varphi-\rho_pD_T\frac{\nabla T}{T}, \tag{36}$$

$$D_B^*=\frac{D_B}{D_{B0}},\ \ D_T^*=\frac{D_T}{D_{T0}},\ \ \varphi^*=\frac{\varphi}{\varphi},\ \ \delta=\frac{T_h-T_c}{T_c}, \tag{37}$$

$$J_p=-\rho_pD_B^*D_{B0}\frac{\nabla}{L}\varphi^*\varphi-\rho_pD_T^*D_{T0}\frac{\nabla[(T_h-T_c)\theta+T_c]}{L[(T_h-T_c)\theta+T_c]}. \tag{38}$$

The dimensionless energy equation is obtained as follows:

$$(\rho C_p)_{nf}\mathbf{v}\cdot\nabla T=\nabla\cdot(k_{nf}\nabla T)-C_{p,p}J_p\cdot\nabla T, \tag{39}$$

$$\begin{aligned}&(\rho C_p)_{nf}\mathbf{V}U_0\frac{\nabla}{L}(T_h-T_c)\theta=\frac{\nabla}{L}\cdot\left(k_{nf}\frac{\nabla}{L}(T_h-T_c)\theta\right)\\&-C_{p,p}\left[-\rho_pD_B^*D_{B0}\frac{\nabla}{L}\varphi^*\varphi-\rho_pD_T^*D_{T0}\frac{\nabla(T_h-T_c)\theta}{L[(T_h-T_c)\theta+T_c]}\right]\frac{\nabla(T_h-T_c)\theta}{L},\end{aligned} \tag{40}$$

$$\begin{aligned}&(\rho C_p)_{nf}\mathbf{V}U_0\frac{\nabla}{L}(T_h-T_c)\theta=\frac{\nabla}{L}\cdot\left(k_{nf}\frac{\nabla}{L}(T_h-T_c)\theta\right)\\&+\left[(\rho C_p)_pD_B^*D_{B0}\frac{\nabla}{L}\varphi^*\varphi+(\rho C_p)_pD_T^*D_{T0}\frac{\nabla(T_h-T_c)\theta}{L((T_h-T_c)\theta+T_c)}\right]\frac{\nabla}{L}(T_h-T_c)\theta,\end{aligned} \tag{41}$$

$$\begin{aligned}&\mathbf{V}\cdot\nabla\theta=\frac{1}{U_0(\rho C_p)_{nf}}\nabla\cdot\left(k_{nf}\frac{\nabla}{L}\theta\right)+\frac{1}{U_0(\rho C_p)_{nf}}\\&\times\left[(\rho C_p)_pD_B^*D_{B0}\frac{\nabla}{L}\varphi^*\varphi+(\rho C_p)_pD_T^*D_{T0}\frac{\nabla(T_h-T_c)\theta}{L((T_h-T_c)\theta+T_c)}\right]\nabla\theta,\end{aligned} \tag{42}$$

$$\mathbf{V}\cdot\nabla\theta=\underbrace{\frac{k_{nf}}{U_0L(\rho C_p)_{nf}}}_{I}\nabla^2\theta+\underbrace{\frac{(\rho C_p)_pD_{B0}\varphi}{(\rho C_p)_{nf}U_0L}}_{II}D_B^*\nabla\varphi^*\cdot\nabla\theta$$
$$+\underbrace{\frac{(\rho C_p)_pD_{T0}(T_h-T_c)}{(\rho C_p)_{nf}U_0L((T_h-T_c)\theta+T_c)}}_{III}D_T^*\nabla\theta\cdot\nabla\theta. \tag{43}$$

By defining non-dimensional parameters in coefficients of energy equation, relations (44)–(46), the compact and non-dimensional form of energy equation will be obtained as relation (49).

$$I=\frac{k_{nf}}{U_0L(\rho C_p)_{nf}}=\frac{k_f(\rho C_p)_f\nu_f}{k_f(\rho C_p)_f\nu_f}\frac{k_{nf}}{U_0L(\rho C_p)_{nf}}$$
$$=\frac{(\rho C_p)_fk_{nf}}{(\rho C_p)_{nf}k_f}\underbrace{\frac{\nu_f}{U_0L}}_{\frac{1}{\mathrm{Re}}}\underbrace{\frac{k_f}{\nu_f(\rho C_p)_f}}_{\frac{1}{\mathrm{Pr}}}=\frac{(\rho C_p)_fk_{nf}}{(\rho C_p)_{nf}k_f}\frac{1}{\mathrm{Re}\,\mathrm{Pr}}, \tag{44}$$

$$II=\frac{k_f\nu_f(\rho C_p)_f}{k_f\nu_f(\rho C_p)_f}\frac{(\rho C_p)_pD_{B0}\varphi}{(\rho C_p)_{nf}U_0L}$$
$$=\frac{(\rho C_p)_p}{(\rho C_p)_{nf}}\underbrace{\frac{\nu_f}{U_0L}}_{\frac{1}{\mathrm{Re}}}\underbrace{\frac{k_f}{\nu_f(\rho C_p)_f}}_{\frac{1}{\mathrm{Pr}}}\underbrace{\frac{(\rho C_p)_f\varphi D_{B0}}{k_f}}_{\frac{1}{Le}}=\frac{(\rho C_p)_p}{(\rho C_p)_{nf}}\frac{1}{\mathrm{Re}\,\mathrm{Pr}\,Le}, \tag{45}$$

$$III=\frac{k_f\nu_f(\rho C_p)_f\varphi D_{B0}T_c}{k_f\nu_f(\rho C_p)_f\varphi D_{B0}T_c}\frac{(\rho C_p)_pD_{T0}(T_h-T_c)}{(\rho C_p)_{nf}U_0L((T_h-T_c)\theta+T_c)}$$
$$=\frac{(\rho C_p)_p}{(\rho C_p)_{nf}}\underbrace{\frac{\nu_f}{U_0L}}_{\frac{1}{\mathrm{Re}}}\underbrace{\frac{k_f}{\nu_f(\rho C_p)_f}}_{\frac{1}{\mathrm{Pr}}}\underbrace{\frac{(\rho C_p)_f\varphi D_{B0}}{k_f}}_{\frac{1}{Le}}\underbrace{\frac{D_{T0}(T_h-T_c)}{\varphi D_{B0}T_c}}_{\frac{1}{N_{BT}}}\underbrace{\frac{1}{\left(1+\frac{T_h-T_c}{T_c}\theta\right)}}_{\frac{1}{1+\delta\theta}}$$
$$=\frac{(\rho C_p)_p}{(\rho C_p)_{nf}}\frac{1}{\mathrm{Re}\cdot\mathrm{Pr}\cdot Le\cdot N_{BT}}\frac{1}{1+\delta\theta}, \tag{46}$$

$$D_{B0}=\frac{k_bT_c}{3\pi\mu_fd_p}, \tag{47}$$

$$D_{T0}=0.26\frac{k_f}{2k_f+k_p}\frac{\mu_f}{\rho_f}\varphi, \tag{48}$$

$$\mathbf{V}\cdot\nabla\theta=\frac{(\rho C_p)_fk_{nf}}{(\rho C_p)_{nf}k_f}\frac{1}{\mathrm{Re}\cdot\mathrm{Pr}}\nabla^2\theta+\frac{(\rho C_p)_p}{(\rho C_p)_{nf}}\frac{D_B^*}{\mathrm{Re}\cdot\mathrm{Pr}\cdot Le}\nabla\varphi^*\cdot\nabla\theta$$
$$+\frac{(\rho C_p)_p}{(\rho C_p)_{nf}}\frac{D_T^*}{\mathrm{Re}\cdot\mathrm{Pr}\cdot Le\cdot N_{BT}}\frac{\nabla\theta\cdot\nabla\theta}{1+\delta\theta}. \tag{49}$$

Also, concentration equation (50), is transformed to its non-dimensional form Eq. (55), via defining non-dimensional parameters in Eqs. 52–54.

$$\mathbf{v}\cdot\nabla\varphi=-\frac{1}{\rho_p}\nabla\cdot J_p=-\frac{1}{\rho_p}\nabla\cdot\left[-\rho_pD_B\nabla\varphi-\rho_pD_T\frac{\nabla T}{T}\right], \tag{50}$$

$$\mathbf{V}U_0\cdot\frac{\nabla}{L}\varphi\varphi^*=\frac{\nabla}{L}\cdot\left[D_B^*D_{B0}\frac{\nabla\varphi\varphi^*}{L}+D_T^*D_{T0}\frac{\nabla((T_h-T_c)\theta+T_c)}{L((T_h-T_c)\theta+T_c)}\right], \tag{51}$$

$$\begin{aligned}\mathbf{V}\cdot\nabla\varphi^{*} &= \nabla\cdot\left[D_B^{*}D_{B0}\frac{\nabla\varphi^{*}}{U_0L}+D_T^{*}D_{T0}\frac{\nabla((T_h-T_c)\theta+T_c)}{U_0L\varphi((T_h-T_c)\theta+T_c)}\right]\\ &= \frac{D_{B0}}{U_0L}D_B^{*}\nabla^2\varphi^{*}+\frac{D_{T0}(T_h-T_c)}{U_0L\varphi}D_T^{*}\frac{\nabla^2\theta}{T_c\left(\left(\frac{T_h-T_c}{T_c}\right)\theta+1\right)}\\ &= \underbrace{\frac{D_{B0}}{U_0L}}_{IV}D_B^{*}\nabla^2\varphi^{*}+\underbrace{\frac{D_{T0}(T_h-T_c)}{U_0L\varphi T_c}}_{V}D_T^{*}\frac{\nabla^2\theta}{1+\delta\theta},\end{aligned} \tag{52}$$

$$IV=\frac{\nu_f}{\nu_f}\frac{D_{B0}}{U_0L}=\underbrace{\frac{\nu_f}{U_0L}}_{\frac{1}{\mathrm{Re}}}\underbrace{\frac{D_{B0}}{\nu_f}}_{\frac{1}{Sc}}=\frac{1}{\mathrm{Re}\cdot Sc}, \tag{53}$$

$$V=\frac{\nu_f D_{B0}}{\nu_f D_{B0}}\frac{D_{T0}(T_h-T_c)}{U_0L\varphi T_c}=\underbrace{\frac{\nu_f}{U_0L}}_{\frac{1}{\mathrm{Re}}}\underbrace{\frac{D_{B0}}{\nu_f}}_{\frac{1}{Sc}}\underbrace{\frac{D_{T0}(T_h-T_c)}{\varphi D_{B0}T_c}}_{\frac{1}{N_{BT}}}=\frac{1}{\mathrm{Re}\cdot Sc\cdot N_{BT}}, \tag{54}$$

$$\mathbf{V}\cdot\nabla\varphi^{*}=\frac{D_B^{*}}{\mathrm{Re}\cdot Sc}\nabla^2\varphi^{*}+\frac{D_T^{*}}{\mathrm{Re}\cdot Sc\cdot N_{BT}}\frac{\nabla^2\theta}{1+\delta\theta}. \tag{55}$$

References

[1] D.K. Devendiran, V.A. Amirtham, A review on preparation, characterization, properties and applications of nanofluids, Renew. Sustain. Energy Rev. 60 (2016) 21–40.

[2] S. Izadi, T. Armaghani, R. Ghasemiasl, A.J. Chamkha, M. Molana, A comprehensive review on mixed convection of nanofluids in various shapes of enclosures, Powder Technol. 343 (2019) 880–907.

[3] A. Rahimi, A.D. Saee, A. Kasaeipoor, E.H. Malekshah, A comprehensive review on natural convection flow and heat transfer, Int. J. Numer. Methods Heat Fluid Flow 29 (3) (2019) 834–877.

[4] P. Khatak, R. Jakhar, M. Kumar, Enhancement in cooling of electronic components by nanofluids, J. Inst. Eng.: Series C 96 (3) (2015) 245–251.

[5] H.K. Gupta, G.D. Agrawal, J. Mathur, Investigations for effect of Al_2O_3–H_2O nanofluid flow rate on the efficiency of direct absorption solar collector, Case Stud. Therm. Eng. 5 (2015) 70–78.

[6] G.H.R. Kefayati, Mesoscopic simulation of mixed convection on non-Newtonian nanofluids in a two sided lid-driven enclosure, Adv. Powder Technol. 26 (2) (2015) 576–588.

[7] A.A. Vasconcelos, A.O.C. Gómez, E.P. Bandarra Filho, J.A.R. Parise, Experimental evaluation of SWCNT-water nanofluid as a secondary fluid in a refrigeration system, Appl. Therm. Eng. 111 (2017) 1487–1492.

[8] G. Kefayati, A.P. Bassom, A lattice Boltzmann method for single-and two-phase models of nanofluids: Newtonian and non-Newtonian nanofluids, Phys. Fluids 33 (10) (2021) 102008.

[9] S.A.M. Mehryan, E. Izadpanahi, M. Ghalambaz, A.J. Chamkha, Mixed convection flow caused by an oscillating cylinder in a square cavity filled with Cu–Al_2O_3/water hybrid nanofluid, J. Therm. Anal. Calorim. 137 (3) (2019) 965–982.

[10] M. Ghalambaz, S.A.M. Mehryan, A. Hajjar, A. Veismoradi, Unsteady natural convection flow of a suspension comprising Nano-Encapsulated Phase Change Materials (NEPCMs) in a porous medium, Adv. Powder Technol. 31 (3) (2020) 954–966.

[11] F. Selimefendigil, H.F. Öztop, Fluid-solid interaction of elastic-step type corrugation effects on the mixed convection of nanofluid in a vented cavity with magnetic field, Int. J. Mech. Sci. 152 (2019) 185–197.

[12] T. Tayebi, H.F. Öztop, A.J. Chamkha, Natural convection and entropy production in hybrid nanofluid filled-annular elliptical cavity with internal heat generation or absorption, Therm. Sci. Eng. Prog. 19 (2020) 100605.

[13] T. Tayebi, A.J. Chamkha, Entropy generation analysis due to MHD natural convection flow in a cavity occupied with hybrid nanofluid and equipped with a conducting hollow cylinder, J. Therm. Anal. Calorim. 139 (3) (2020) 2165–2179.

[14] F. Selimefendigil, H.F. Öztop, Combined effects of double rotating cones and magnetic field on the mixed convection of nanofluid in a porous 3D U-bend, Int. Commun. Heat Mass Tran. 116 (2020) 104703.

[15] F. Selimefendigil, H.F. Öztop, A.J. Chamkha, Analysis of mixed convection of nanofluid in a 3D lid-driven trapezoidal cavity with flexible side surfaces and inner cylinder, Int. Commun. Heat Mass Tran. 87 (2017) 40–51.

[16] M.A. Ismael, E. Abu-Nada, A.J. Chamkha, Mixed convection in a square cavity filled with CuO-water nanofluid heated by corner heater, Int. J. Mech. Sci. 133 (2017) 42–50.

[17] A.M. Rashad, M.A. Ismael, A.J. Chamkha, M.A. Mansour, MHD mixed convection of localized heat source/sink in a nanofluid-filled lid-driven square cavity with partial slip, J. Taiwan Inst. Chem. Eng. 68 (2016) 173–186.

[18] M.A. Ismael, M.A. Mansour, A.J. Chamkha, A.M. Rashad, Mixed convection in a nanofluid filled-cavity with partial slip subjected to constant heat flux and inclined magnetic field, J. Magn. Magn Mater. 416 (2016) 25–36.

[19] M. Sheikholeslami, A.J. Chamkha, Flow and convective heat transfer of a ferro-nanofluid in a double-sided lid-driven cavity with a wavy wall in the presence of a variable magnetic field, Numer. Heat Tran., Part A: Applications 69 (10) (2016) 1186–1200.

[20] H.F. Oztop, K. Al-Salem, I. Pop, MHD mixed convection in a lid-driven cavity with corner heater, Int. J. Heat Mass Tran. 54 (15–16) (2011) 3494–3504.

[21] A.M. Rashad, T. Armaghani, A.J. Chamkha, M.A. Mansour, Entropy generation and MHD natural convection of a nanofluid in an inclined square porous cavity: effects of a heat sink and source size and location, Chin. J. Phys. 56 (1) (2018) 193–211.

[22] A.I. Alsabery, R. Mohebbi, A.J. Chamkha, I. Hashim, Effect of local thermal non-equilibrium model on natural convection in a nanofluid-filled wavy-walled porous cavity containing inner solid cylinder, Chem. Eng. Sci. 201 (2019) 247–263.

[23] M. Sheikholeslami, Influence of Lorentz forces on nanofluid flow in a porous cavity by means of non-Darcy model, Eng. Comput. 34 (8) (2017) 2651–2667.

[24] A.S. Dogonchi, S.M. Seyyedi, M. Hashemi-Tilehnoee, A.J. Chamkha, D.D. Ganji, Investigation of natural convection of magnetic nanofluid in an enclosure with a porous medium considering Brownian motion, Case Stud. Therm. Eng. 14 (2019) 100502.
[25] J. Buongiorno, Convective transport in nanofluids, J. Heat Tran. 128 (3) (2006) 240–250.
[26] D. Wen, Y. Ding, Experimental investigation into convective heat transfer of nanofluids at the entrance region under laminar flow conditions, Int. J. Heat Mass Tran. 47 (24) (2004) 5181–5188.
[27] G. Kefayati, Mixed convection of non-Newtonian nanofluid in an enclosure using Buongiorno's mathematical model, Int. J. Heat Mass Tran. 108 (2017) 1481–1500.
[28] G. Kefayati, A two-and three-dimensional mesoscopic method for an updated non-homogeneous model of Newtonian and non-Newtonian nanofluids, Phys. Fluids 34 (3) (2022), 032003.
[29] I. Hashim, A.I. Alsabery, M.A. Sheremet, A.J. Chamkha, Numerical investigation of natural convection of Al_2O_3-water nanofluid in a wavy cavity with conductive inner block using Buongiorno's two-phase model, Adv. Powder Technol. 30 (2) (2019) 399–414.
[30] A.I. Alsabery, T. Armaghani, A.J. Chamkha, I. Hashim, Two-phase nanofluid model and magnetic field effects on mixed convection in a lid-driven cavity containing heated triangular wall, Alex. Eng. J. 59 (1) (2020) 129–148.
[31] P. Barnoon, D. Toghraie, R.B. Dehkordi, H. Abed, MHD mixed convection and entropy generation in a lid-driven cavity with rotating cylinders filled by a nanofluid using two phase mixture model, J. Magn. Magn Mater. 483 (2019) 224–248.
[32] M.R.D. Garmroodi, A. Ahmadpour, F. Talati, MHD mixed convection of nanofluids in the presence of multiple rotating cylinders in different configurations: a two-phase numerical study, Int. J. Mech. Sci. 150 (2019) 247–264.
[33] M.A. Sheremet, I. Pop, Mixed convection in a lid-driven square cavity filled by a nanofluid: Buongiorno's mathematical model, Appl. Math. Comput. 266 (2015) 792–808.
[34] M. Esfandiary, B. Mehmandoust, A. Karimipour, H.A. Pakravan, Natural convection of Al_2O_3-water nanofluid in an inclined enclosure with the effects of slip velocity mechanisms: Brownian motion and thermophoresis phenomenon, Int. J. Therm. Sci. 105 (2016) 137–158.
[35] S.Y. Motlagh, H. Soltanipour, Natural convection of Al_2O_3-water nanofluid in an inclined cavity using Buongiorno's two-phase model, Int. J. Therm. Sci. 111 (2017) 310–320.
[36] A.I. Alsabery, T. Armaghani, A.J. Chamkha, M.A. Sadiq, I. Hashim, Effects of two-phase nanofluid model on convection in a double lid-driven cavity in the presence of a magnetic field, Int. J. Numer. Methods Heat Fluid Flow 29 (4) (2019) 1272–1299.
[37] M. Izadi, S. Sinaei, S.A.M. Mehryan, H.F. Oztop, N. Abu-Hamdeh, Natural convection of a nanofluid between two eccentric cylinders saturated by porous material: Buongiorno's two phase model, Int. J. Heat Mass Tran. 127 (2018) 67–75.
[38] M. Izadi, G. Hoghoughi, R. Mohebbi, M. Sheremet, Nanoparticle migration and natural convection heat transfer of Cu-water nanofluid inside a porous undulant-wall enclosure using LTNE and two-phase model, J. Mol. Liq. 261 (2018) 357–372.
[39] M. Corcione, Empirical correlating equations for predicting the effective thermal conductivity and dynamic viscosity of nanofluids, Energy Convers. Manag. 52 (1) (2011) 789–793.
[40] M. Paroncini, F. Corvaro, Natural convection in a square enclosure with a hot source, Int. J. Therm. Sci. 48 (9) (2009) 1683–1695.
[41] M. Corcione, M. Cianfrini, A. Quintino, Two-phase mixture modeling of natural convection of nanofluids with temperature-dependent properties, Int. J. Therm. Sci. 71 (2013) 182–195.
[42] L. Wang, X. Yang, C. Huang, Z. Chai, B. Shi, Hybrid lattice Boltzmann-TVD simulation of natural convection of nanofluids in a partially heated square cavity using Buongiorno's model, Appl. Therm. Eng. 146 (2019) 318–327.